Mobile metal adatoms on single layer, bilayer, and trilayer graphene: An *ab initio* DFT study with van der Waals corrections correlated with electron microscopy data

T. P. Hardcastle,[1,*] C. R. Seabourne,[1] R. Zan,[2,3] R. M. D. Brydson,[1] U. Bangert,[2] Q. M. Ramasse,[4] K. S. Novoselov,[3] and A. J. Scott[1,†]

[1]*Institute for Materials Research, SPEME, University of Leeds, Leeds LS2 9JT, United Kingdom*
[2]*School of Materials, University of Manchester, Manchester, M13 9PL, United Kingdom*
[3]*School of Physics and Astronomy, University of Manchester, Manchester, M13 9PL, United Kingdom*
[4]*SuperSTEM Laboratory, STFC Daresbury Campus, Daresbury, WA4 4AD, United Kingdom*

(Received 14 November 2012; revised manuscript received 5 March 2013; published 17 May 2013)

The plane-wave density functional theory code CASTEP was used with the Tkatchenko-Scheffler van der Waals correction scheme and the generalized gradient approximation of Perdew, Burke, and Ernzerhof (GGA PBE) to calculate the binding energy of Au, Cr, and Al atoms on the armchair and zigzag edge binding sites of monolayer graphene, and at the high-symmetry adsorption sites of single layer, bilayer, and trilayer graphene. All edge site binding energies were found to be substantially higher than the adsorption energies for all metals. The adatom migration activation barriers for the lowest energy migration paths on pristine monolayer, bilayer, and trilayer graphene were then calculated and found to be smaller than or within an order of magnitude of k_BT at room temperature, implying very high mobility for all adatoms studied. This suggests that metal atoms evaporated onto graphene samples quickly migrate across the lattice and bind to the energetically favorable edge sites before being characterized in the microscope. We then prove this notion for Al and Au on graphene with scanning transmission electron microscopy (STEM) images showing that these atoms are observed exclusively at edge sites, and also hydrocarbon-contaminated regions, where the pristine regions of the lattice are completely devoid of adatoms. Additionally, we review the issue of fixing selected atomic positions during geometry optimization calculations for graphene/adatom systems and suggest a guiding principle for future studies.

DOI: 10.1103/PhysRevB.87.195430 PACS number(s): 81.05.ue, 71.15.Mb, 68.37.Ma, 68.43.−h

I. INTRODUCTION

A. Overview of recent theoretical studies of graphene-metal systems

The original synthesis of graphene[1] has subsequently sparked worldwide attention owing to its potential to revolutionize many areas of industry. Nanoelectronics is one such promising area, in which interfacing graphene via metal adatom/cluster contacts is a recurring theme.[2–8] This area of research is still developing and the consequences of particular dopants on the electronic properties of graphene are still being investigated. Widespread implementation of graphene-based electronics will therefore involve developing a more detailed understanding of metal-graphene interactions on a fundamental level. To this end, many theoretical studies using density functional theory (DFT) have already emerged which present predictions of binding energies and relaxed structures of various metal adatoms and clusters on pristine single layer graphene[9–24] and on graphene defect structures.[25–31] Potential contacting applications will depend very much on the metal used because vacancy formation energies can be greatly reduced by certain dopants. In 2010, Karoui *et al.*[31] predicted that a Ni substrate assists graphene in healing its vacancy defects. In contrast, Boukhvalov and Katsnelson[26] predicted in 2009 that Fe, Ni, and Co adatoms dramatically reduce vacancy formation energies in graphene, destroying it in the process. In this latter study Au atoms were predicted to have almost no effect on graphene vacancy formation energies, thus preserving its strength. We recently observed nanoscale holes being etched into pristine regions of graphene by various metal adatoms, with the exception of Au for which no etching process was seen to occur.[32]

Trends have emerged regarding the preferred binding sites for metal adatoms on graphene at absolute zero. Recent DFT studies[11,14–16] predict that transition metals generally adsorb at the hollow (H) site (see Fig. 3). Au atoms have been predicted to adsorb preferentially to the atop (A) site.[11,16,17] It can be easy to erroneously conclude from these studies that one would expect stable and static configurations for these adatoms to exist on the basis of the local energetic minima predicted by geometry optimization calculations at absolute zero. However, the calculated absolute difference in binding energy between adsorption sites is often very small, so it is sensible to suggest from these studies alone that the activation barriers for adatom migration are also small; small enough that the perturbing effects of room temperature, $T \sim 300$ K, cause certain metal adatoms to be highly mobile on graphene at room temperature.[14,16,29]

DFT-calculated adatom binding energies are very sensitive to the exchange correlation functional used. To illustrate this, Table I shows binding energies of a single Au adatom on pristine single layer graphene taken from some recent *ab initio* DFT studies.[9,10,12,17,18,25] The local density approximation (LDA) functional is well known to significantly overbind compared to the generalized gradient approximation as parametrized by Perdew, Burke, and Ernzerhof[36] (GGA PBE). This is evident from the values shown in Table I. Despite the widespread success of the GGA PBE functional, it fails to accurately simulate nonlocal correlation effects which dominate in many biological and chemical systems. These systems are characterized by weak long-ranged interactions between instantaneous multipoles occurring in the electron density, collectively and commonly referred to as van der Waals forces. The GGA PBE functional also fails to simulate

TABLE I. Recently published DFT-calculated Au adatom/graphene binding energies on the three high symmetry adsorption sites of single layer graphene. Negative binding energies signify that the configurations are stable, as per Eq. (1.1).

Binding energy E_b of Au adatom on pristine single layer graphene/eV. All values quoted to 3 d.p. unless otherwise specified.									
XC Functional	LDA			GGA PBE			GGA PBE van der Waals-corrected (correction scheme used)		
Author	Atop (A)	Bridge (B)	Hollow (H)	Atop (A)	Bridge (B)	Hollow (H)	Atop (A)	Bridge (B)	Hollow (H)
Lima[9]	–	–	–	− 0.410	–	–	–	–	–
Tang[25]	–	–	–	− 0.075	–	–	–	–	–
Ding[10]	− 0.77 (2 d.p.)	–	− 0.50 (2 d.p.)	− 0.16 (2 d.p.)	–	− 0.16 (2 d.p.)	–	–	–
Varns and Strange[12]	− 0.79 (2 d.p.)	− 0.74 (2 d.p.)	− 0.52 (2 d.p.)	–	–	–	–	–	–
Chan[17]	–	–	–	− 0.096	− 0.089	− 0.085	–	–	–
Amft[18]	− 0.732	− 0.698	− 0.451	− 0.099	− 0.081	no bond	− 0.385 (Dion *et al.*[38–40]) − 0.886 (Grimme[37])	− 0.314 (Dion *et al.*[38–40]) − 0.881 (Grimme[37])	− 0.322 (Dion *et al.*[38–40]) − 0.870 (Grimme[37])

interlayer interactions in graphite and multilayer graphene, thereby making noncorrected GGA functionals inappropriate for modeling involving structural relaxation of the systems in this paper. GGA-type van der Waals correction schemes for implementation into DFT codes have been designed by Grimme,[37] Dion and Rydberg,[38–40] Jurečka *et al.*,[41] and Tkatchenko and Scheffler[42] (TS). These correction schemes allow for new insight to be gained into possible surface physisorption bonding mechanisms between graphene and metal adatoms; an effect which is impossible to probe with the native LDA and GGA PBE functionals employed in virtually all DFT studies so far published. Moreover, van der Waals-corrected DFT sheds light on the graphene-metal interaction, not least because physisorption may be involved, but also because many laboratory synthesis methods produce samples containing regions which are multilayered[32–35,43–46] and are therefore graphitic in character. To our knowledge, only two *ab initio* DFT studies, by Amft *et al.*[18] and Ming *et al.*,[47] have incorporated nonlocal correlation effects with graphene/graphite-metal adatom systems. Amft *et al.*[18] used the GGA-type correction schemes of Grimme[37] and Dion and Rydberg[38–40] on single layer graphene/metal systems, and their values shown here in Table I aptly demonstrate the drastic effect of including these interactions.

B. Electron microscopy studies of graphene-metal systems

While theoretical studies of graphene-metal systems are ubiquitous, a significant experimental insight of this system has recently emerged from a series of images obtained by our group[32–35] using aberration-corrected scanning transmission electron microscopy (AC STEM) at 60 keV, examples of which are presented in Fig. 1. In these studies, high angle annular dark field (HAADF) imaging was used to produce images which clearly showed suspended monolayer graphene membranes consisting of pristine regions along with defective and hydrocarbon-contaminated regions, onto which various metal adatoms had been evaporated. As Fig. 1 shows, Au and Al atoms are observed exclusively at edge sites on the perimeters of etched holes or are clustered at hydrocarbon-contaminated regions. No metal adatoms were ever observed on these samples. A sample of variable thickness consisting of monolayer and multilayer regions and evaporated with Au was also prepared. By following the method of Eberlein *et al.*,[48] electron energy loss spectra (EELS) were used to identify the monolayer, bilayer, and trilayer regions unambiguously for this sample. The remaining regions were collectively identified as consisting of four or more layers. A very small number of isolated Au adatoms were found momentarily on the pristine regions of this sample, but only on areas whose thickness could be unambiguously identified as four or more layers. By using the approximate proportionality of the image intensity to the square of the atomic number Z, the adsorption positions of these Au adatoms were determined, and found to be consistently at atop sites. In these studies we speculated that the graphene-metal binding energy may be significantly higher for thicker samples on account of the van der Waals-type contribution from the sublayers. We also speculated that all metal adatoms were very mobile on all of our samples and had migrated to defective and contaminated regions, presumed to be more stable, before the samples were characterized in the microscope.

Thus, the first aim of this paper is to use van der Waals-corrected DFT to predict the binding energy of selected metal adatoms at the high symmetry sites of pristine regions of graphene, and at the most commonly observed monolayer edge defects, in order to compare the energetic stability of these regions. The second aim is then to investigate adatom mobility on the pristine substrates by directly sampling the energy landscape corresponding to intermediate configurations between high symmetry adsorption sites in order to locate the transition state saddle points and thus evaluate the migration activation barriers. The van der Waals corrections will produce explicit and original evidence of how adatom binding energy and mobility changes with increasing graphene substrate thickness, if at all. To our knowledge, this is the first DFT study of a multilayer graphene-metal interaction to make a direct comparison with STEM data, the first study to calculate adatom migration barriers on both monolayer

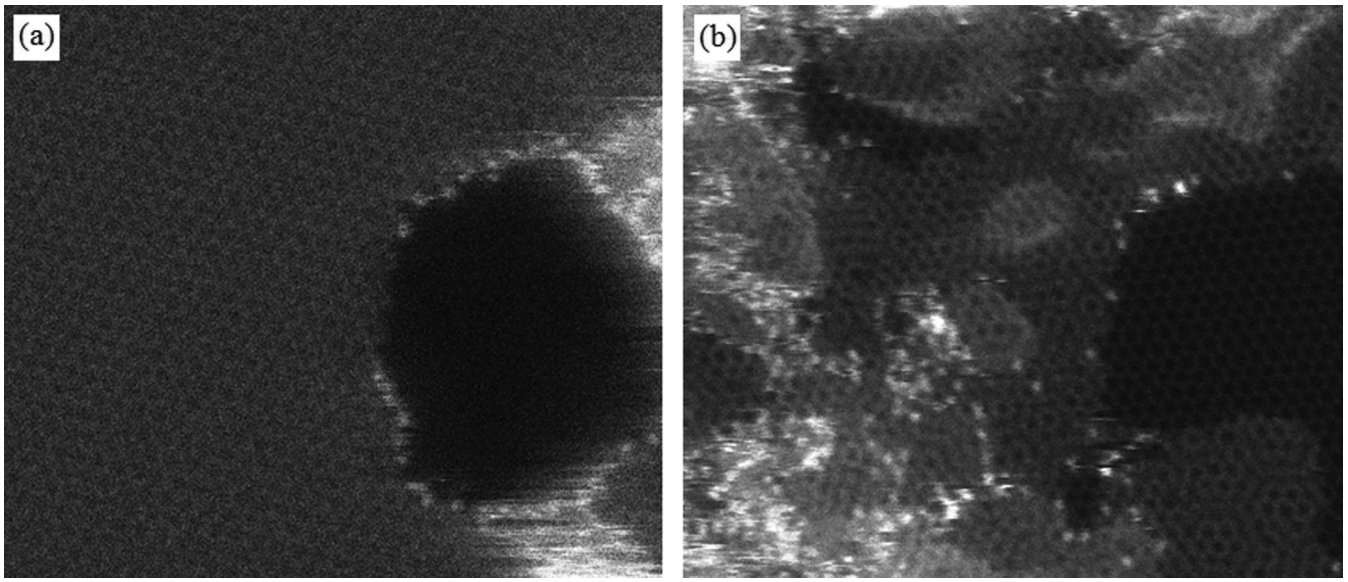

FIG. 1. STEM HAADF images at 60 keV showing preferential binding of metal atoms to edge defects, hydrocarbon-contaminated regions, and metal clusters. (a) Monolayer graphene sheet with hole, onto which a 2 Å layer of Al was evaporated. Al atoms are seen only at edge sites and in clusters near the hole.[35] (b) Monolayer graphene sheet with bilayer and trilayer regions onto which a 5 Å layer of Au gold was evaporated. Individual Au atoms and Si contaminants (of less bright contrast) clearly bind preferentially to edge sites. The pristine regions of the lattice are completely devoid of adatoms in both cases.

and multilayer graphene (real STEM specimens consist of multilayer regions in addition to single layers), and also the first such study to incorporate the van der Waals correction scheme of Tkatchenko and Scheffler.[42] In addition, we also address the apparent lack of agreement in the fixing of atomic positions during geometry optimization calculations, a discussion of which now follows.

C. Discussion on long-ranged adatom-induced lattice perturbations and the constraining of atomic positions during geometry optimization

The essence of the approximation with graphene adsorption studies is attempting to simulate the asymptotic flatness and stiffness of graphene far from the adsorbate, while accounting for the fact that adsorbate-induced lattice perturbations can be long ranged, all under the constraints of finite supercell sizes dictated by the efficient use of shared computing architectures. (Real graphene is known to have ripples under typical laboratory conditions,[49,50] but we neglect these effects here as the period of these oscillations is relatively large.)

Lambin *et al.*[51] recently demonstrated that for the case of nitrogen substitutional dopants in graphene with the LDA functional, the calculated local density of states differs significantly for 9×9 and 10×10 supercells. Although adatom-induced lattice perturbations are likely to be smaller than those of substitutional dopants, the convergence of adatom binding energy should ideally be tested with supercell size, or the error due to the use of finite supercell sizes should at least be estimated. We carried out some tests using the LDA functional with 4×4 supercells with Au and Cr adatoms placed in the center, in which all carbon atoms were relaxed. We found out-of-plane lattice perturbations to be significant at the supercell boundaries far from the adatom in response to the localized puckering near the adatom. This raises the question of whether such undulating structures are a physically meaningful simulation of graphene at all. Also, there is no well-defined way of measuring the distance of the adsorbate above the graphene plane in these systems. Despite it being something of an artifice, we advocate that fixing the positions of selected carbon atoms far from the adatom is a pragmatic way to simulate the stiffness and flatness of pristine graphene far from the adsorbate, but only if the supercells used are large enough to account for lattice perturbations to a justifiable level of energy convergence.

Further on the issue of fixing atomic positions, there appears to be no general consensus on the issue of *which* atomic positions should be fixed. We take the opportunity now to list the conventions used in recently published studies to illustrate the disparity, and then suggest a simple guiding principle for future studies. In the study by Sargolzaei and Gudarzi,[13] the positions of the adatom and the first nearest-neighbor carbon atoms were relaxed, with all other carbon positions fixed. Ding *et al.*[10] state that they allowed all atomic positions to relax in the direction normal to the graphene plane, but it is unclear whether they also allowed for in-plane relaxations. Tang *et al.*[25] allowed all atoms in the calculation to relax in all directions. Amft *et al.*[18] appear to have used the still different method of fixing the positions of the adatom and the carbon atoms on the supercell perimeter, while all other carbon positions were allowed to relaxed. Nakada *et al.*[14] used yet another method and allowed all atoms to relax except for just one carbon atom far from the adatom, with the adatom only allowed to relax in the z (vacuum) direction. While these different choices may or may not result in negligible differences in calculated binding energies for a given supercell size, most of them can introduce the easily avoidable idiosyncrasy of breaking the symmetry of the system. This is illustrated in Fig. 2 which

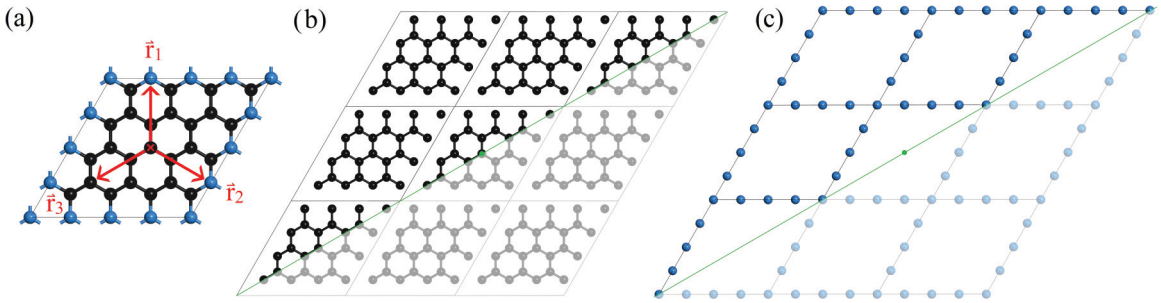

FIG. 2. (Color online) Symmetry breaking caused by fixing atoms on the supercell perimeter without appealing to lattice symmetries. (a) The lattice environment experienced by the adatom along directions $\vec{r}_3$ is different to that along $\vec{r}_1$ and $\vec{r}_2$, despite these directions being crystallographically equivalent. (b) The resulting twofold rotational symmetry of the unfixed carbon sublattice and (c) the twofold rotational symmetry of the fixed carbon sublattice about the axis passing through the adsorption site.

shows a 32 atom graphene monolayer supercell and the atop adsorption site (A) indicated with a red cross in the center of the supercell. The C atoms on the supercell perimeter are indicated in blue to signify that their positions are fixed, whilet all remaining C atoms indicated in black are allowed to relax. By fixing the atoms indicated, the lattice environment encountered along the directions $\vec{r}_1$ and $\vec{r}_2$ is not the same as that along the direction $\vec{r}_3$, despite the fact that these three directions are all supposed to be crystallographically equivalent. In fact, the resulting sublattices consisting of fixed and unfixed C atoms each have twofold rotational symmetry about the adsorption site as shown in Figs. 2(b) and 2(c), in contradiction with the threefold rotational symmetry of the complete lattice about the adsorption site. To restore the symmetry and create an environment for the adatom which is unbiased, we select C atoms to be fixed in our supercells so that (i) C atoms which are fixed form a sublattice which shares the rotational symmetry of the complete lattice about the axis passing through the adsorption site of interest and (ii) all of the remaining unfixed C atoms form a sublattice which shares the rotational symmetry of the complete lattice about that same axis. This is illustrated in Figs. 9 and 10 (Appendix).

D. Binding sites, binding energy, and electrostatic dipole corrections

For the pristine regions, we confine our attention to the high symmetry points lying at the vertices of the symmetry-reduced Wigner-Seitz cells of the single and multilayer systems as indicated in Figs. 3(a) and 3(b). For lattice edges, the boundaries separating irreducible regions of the "zigzag" and "armchair" edges indicated in Figs. 3(c) and 3(d) are considered for the monolayer case for each of the three metals tested. The binding energy E_b at site X—where X takes the value X = A,A_1,A_2,B, H for adsorption sites, or C_1, C_2, Z_1, Z_2 for edge defect sites as appropriate—is defined in the conventional way as the difference in enthalpy of the composite system supercell and that of the sum of the two isolated system supercells:

$$E_b\,(\mathrm{X}) = E_{C+m}\,(\mathrm{X}) - E_m - E_C, \qquad (1.1)$$

where E_{C+m} is the TS-corrected enthalpy of the geometry-optimized graphene/metal supercell and E_m and E_C are the TS-corrected enthalpies of the isolated metal and geometry-optimized graphene supercells, respectively.

One subtle but essential physical ingredient which can interfere with adsorption calculations is that of electrostatic polarity under periodic boundary conditions (PBC). A well-known difficulty which dates back to classical electrostatics is that the polarization of an ionic crystal can depend on the definition of the (neutral) bulk unit cell if no explicit reference is made to the surface conditions. This has been expressed with great clarity in the context of *ab initio* calculations by Makov and Payne.[52] Under the constraints of PBC, the crystal is infinite so the surface is undefined. Thus, with no surface cell to cancel out the spurious potential produced from unphysical interactions between periodic images of multipole moments in neighboring supercells, the dipole moment of a neutral polar system can depend on the location of the supercell boundaries, or equivalently, on the placement of the system within the supercell. This positional dependence of the energy arises because of electron density overlapping with the cell boundary in the direction of the polarity, thus making the total cell dipole sensitive to the placement of the system. Metal adatom-graphene systems, especially adsorption configurations, tend to be polar in the vacuum direction owing to the charge transfer associated with the metal-carbon bond. Hence, it is essential that the systems are placed in the center of the vacuum slab far from the supercell boundary at each end of the vacuum so as to ensure that the charge density is zero across this boundary. Various dipole correction schemes and studies of the subject have been published.[53–59] In this work we use the self-consistent electrostatic dipole correction scheme of Neugebaueur and Scheffler[53] as implemented in CASTEP[60] to ensure that our input files satisfy the condition of zero charge density at the extremities of the vacuum slab.

II. METHOD

A. Exchange correlation functional, basis set parameters, optimization of isolated structures, and energy/enthalpy convergence with cell dimensions

Two van der Waals-corrected cell-optimized geometry optimization calculations were carried out on the bulk graphite unit cell using the plane wave density functional theory code CASTEP[60] with the GGA PBE functional,[36] Vanderbilt ultrasoft pseudopotentials,[61] and a temporary hyperfine

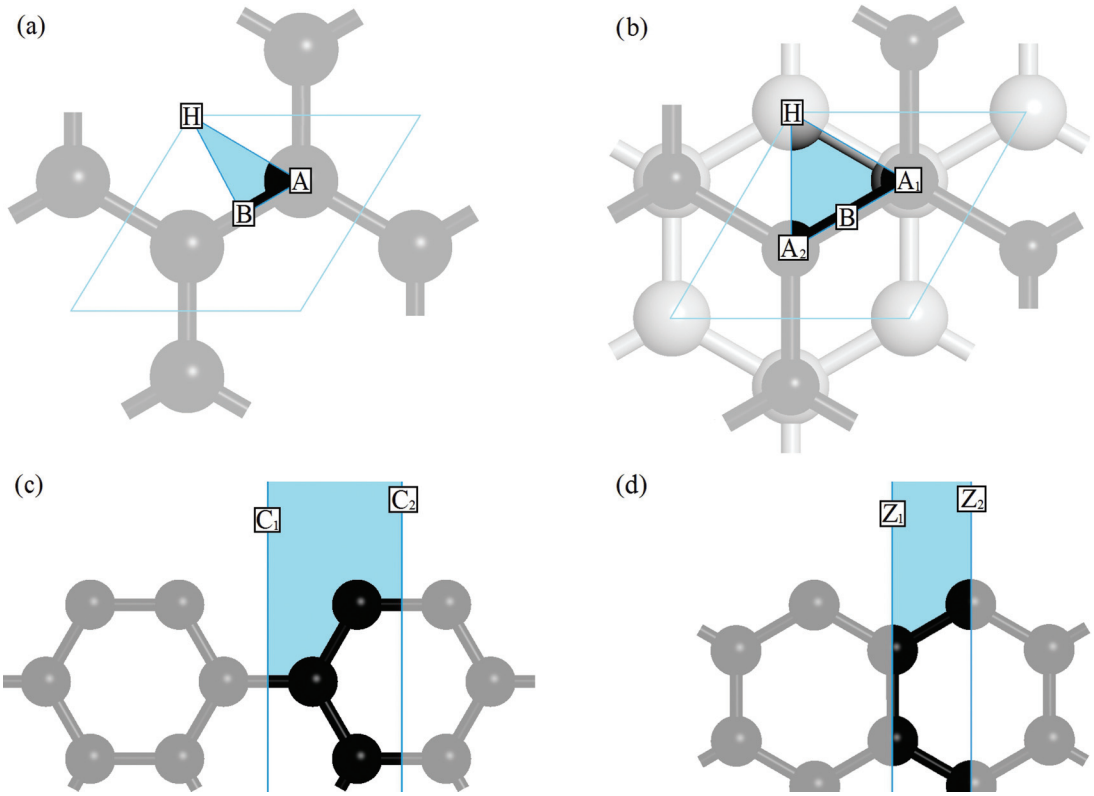

FIG. 3. (Color online) The high symmetry adsorption sites located at the vertices of the symmetry-reduced Wigner Seitz cell boundaries for (a) single layer graphene and (b) 2+ layer graphene, for which AB stacking is assumed. In the multilayer case, the top layer is represented by small black balls and sticks and the sublayer is represented by large grey balls and sticks. (c) and (d) The high symmetry binding sites of the monolayer armchair edge and zigzag edge considered in this work.

basis set. The TS van der Waals correction scheme[42] as implemented in CASTEP[60,62] was used for the first calculation and the Grimme scheme[37] for the second. The fully optimized Grimme-corrected final interlayer spacing was found to be 3.27 Å (3 s.f.), whereas the TS-corrected interlayer spacing was found to be 3.32 Å (3 s.f.); considerably closer to the experimentally measured[63] value of 3.35 Å. TS-corrected GGA PBE zero-point energy calculations were then carried out to numerically converge the binding energy of a series of small graphene-metal systems, akin to those shown in Fig. 8(d) (Appendix), with respect to the kinetic energy cutoff E_C and k point spacings s^i (where $i = 1,2,3$ denotes correspondence to the reciprocal lattice vector b_i). A regular Monkhorst-Pack[64] k points grid was used in all cases, and for all subsequent calculations. The k point spacings were converged independently along in-plane and out-of-plane directions to ensure that any subtle behavior at the Dirac points was captured to a satisfactory level of precision. On the basis of these calculations, the kinetic energy cutoff E_C and k point spacings s^i were picked at values satisfying $E_C = 550$ eV and $s^i < 0.035$ Å^{-1}. The TS/Grimme bulk lattice parameter validation test just described was then repeated with this basis set and both correction schemes were verified to produce the same interlayer spacings as before. The TS correction scheme was then chosen along with the established basis set parameters $E_C = 550$ eV and $s^i < 0.035$ Å^{-1} for all subsequent calculations in the paper. Following this, the monolayer, bilayer, and trilayer graphene unit cells were fully thermodynamically optimized with respect to bond lengths, vacuum thicknesses, and layer spacings individually in each case using geometry optimization calculations. The energy of isolated metal atom supercells and the binding energy of composite graphene/metal systems were converged with increasing supercell size in order to determine the required supercell dimensions for each system studied in this work. An exhaustive technical account of this procedure is given in the Appendix.

B. Adsorption site and defect site binding energy calculations

For the adsorption sites, the three monolayer graphene supercells shown in Figs. 9(a)–9(c) (Appendix) were built, and a metal atom of species m = Au, Al, Cr was placed into the center of each supercell at an initial distance of 2 Å above the graphene sheet, to make nine supercells. The positions of the carbon atoms indicated in blue were fixed along all directions, and the positions of the adatom and carbon atoms indicated in black were allowed to relax in all directions. Two and three layer versions of the four types of multilayer supercells shown in Figs. 10(a)–10(d) (Appendix) were then constructed in an identical fashion for each of the three metals m = Au, Al, Cr, to make 24 more supercells. The carbon atom positions were fixed in the multilayer cases by simply applying the reasoning used for the monolayer cases independently

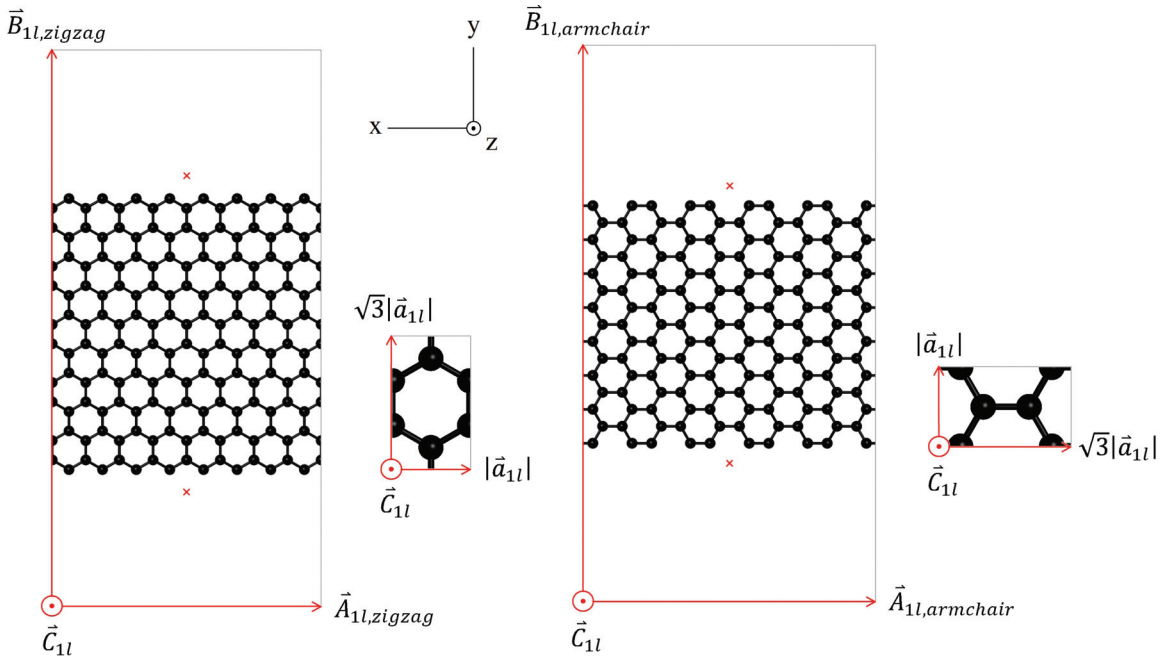

FIG. 4. (Color online) Example supercells used for metal binding to monolayer edges with accompanying unit cells. $|\vec{A}_{1l,\text{zigzag}}| = 8|\vec{a}_{1l}|$ Å, $|\vec{B}_{1l,\text{zigzag}}| = 5\sqrt{3}|\vec{a}_{1l}| + 20$ Å, $|\vec{A}_{1l,\text{armchair}}| = 5\sqrt{3}|\vec{a}_{1l}|$ Å, and $|\vec{B}_{1l,\text{armchair}}| = 7|\vec{a}_{1l}| + 20$ Å.

to each carbon layer. All lattice parameters were fixed at the values indicated in Figs. 9 and 10 (Appendix). For the edge defect sites, four supercells like those shown in Fig. 4 were used, one for each of the four edge sites, whose lattice parameters were all fixed, and in which all atomic positions were relaxed with the metal atom placed 2 Å from the nearest carbon atom(s). These were duplicated into three copies, one set for each metal, to make 12 supercells. To curtail the risk of any of these systems failing to relax into an energetic minimum as a consequence of initial high symmetry, all systems were created with $P1$ symmetry and all symmetry finders were disabled. In addition to this, each metal atom was then offset from its initial site by 0.01 Å in the x direction.

The plane wave DFT code CASTEP[60] was then used with the TS van der Waals correction implementation[62] and Vanderbilt ultrasoft pseudopotentials[61] to carry out spin-polarized geometry optimization calculations for each of these 45 supercells. Valence states incorporated were $2s^2\ 2p^2$ for C, $5d^{10}\ 6s^1$ for Au, $3s^2\ 3p^6\ 3d^5\ 4s^1$ for Cr, and $3s^2\ 3p^1$ for Al. To satisfy the k-points spacings convergence criterion $s^i < 0.035$ Å^{-1}, determined in Sec. II A, a regular and uniformly weighted $3 \times 3 \times 2$ Monkhorst-Pack[64] grid of 9 k points was used to sample the Brillouin zone for the migration supercells illustrated in Fig. 5 and the adsorption supercells in Figs. 9 and 10 (Appendix). For the edge binding supercells illustrated in Fig. 4, a $1 \times 2 \times 2$ grid totalling 2 k points was used. For each series of self-consistent field (SCF) cycles used for the electronic minimization, the exit criterion was imposed that the change in total electron energy between successive SCF cycles be converged to within 5×10^{-7} eV. For the geometry optimization, the Broyden-Fletcher-Goldfarb-Shanno (BFGS) optimization algorithm[65–69] was used with the following three convergence criteria: (i) that the maximum force on all atoms be less than 0.01 eV Å^{-1}, (ii) that the maximum change in position for all atoms between successive BFGS steps be less than 5×10^{-4} Å, and (iii) that the maximum change

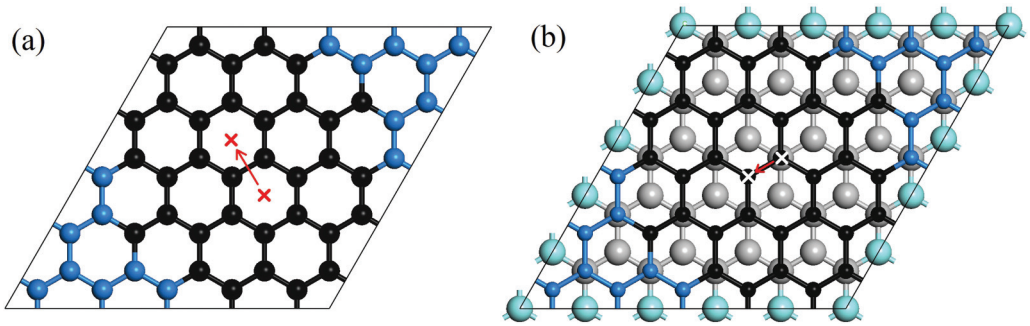

FIG. 5. (Color online) Example supercells used for migration activation barrier calculations. (a) H → B → H trajectory used for Cr and Al on the monolayer and (b) A_1 → B → A_2 trajectory used for Au.

in the total system enthalpy between successive BFGS steps be less than 5×10^{-6} eV per atom. The final TS-corrected enthalpies of these relaxed structures were then recorded as the values of E_{C+m} (X) for insertion into Eq. (1.1). The values E_m and E_C were then calculated for insertion into Eq. (1.1), and the following measures were taken to exploit k-point error cancellation. First, to evaluate the quantities E_m, the 45 final relaxed structure files were duplicated, and the copies were imported back into our visualization software. All of the carbon atoms were then deleted, leaving just the metal atom(s) left in its final position in each case, and a spin-polarized TS-corrected total energy calculation was then performed for each of these 45 isolated metal atoms to evaluate the quantity E_m for each supercell separately. To evaluate the quantities E_C in Eq. (1.1) for the adsorption energies, the spin-polarized TS-corrected isolated graphene energies were calculated using the initial input supercells (i.e., pregeometry optimization), from which the metal atom was deleted in each case. For the edge site binding energies, the isolated graphene edge structures were fully relaxed to obtain spin-polarized TS-corrected enthalpy values E_C. These values were substituted into Eq. (1.1) to give the relaxed structure binding energies E_b (X), which are plotted in Fig. 6.

In order to estimate the error in the final values of adsorption binding energies owing to adatom-induced lattice perturbations, the binding energies of three fully relaxed 8×8 supercells were calculated; one for each metal. The binding energies for Cr and Al agreed with those of the 5×5 supercells up to a maximum discrepancy of 0.024 and 0.018 eV, respectively, with a slightly larger maximum discrepancy of 0.056 eV recorded for the case of Au. These tests confirmed that while the calculated binding energies were likely to be somewhat underestimated owing to the limited supercell sizes employed in this study, the lattice perturbations for the adatoms studied were not significant enough to have an overriding influence on the main conclusions. Though the various approaches in this paper are computationally expensive (using large supercells and detailed basis sets), their rigorous nature and thorough design is beyond routine, novel, and necessary to minimize errors and correctly account for often small energy differences.

C. Adatom migration activation barriers

Using the adsorption binding energy results of the next section, the migration pathways H → B → H on all substrates were identified as obvious candidates for initial guesses of the lowest energy adatom diffusion pathways for Cr and Al, along with the paths A → B → A ($A_1 \rightarrow B \rightarrow A_2$) on the monolayer (multilayer) substrates for Au. These paths

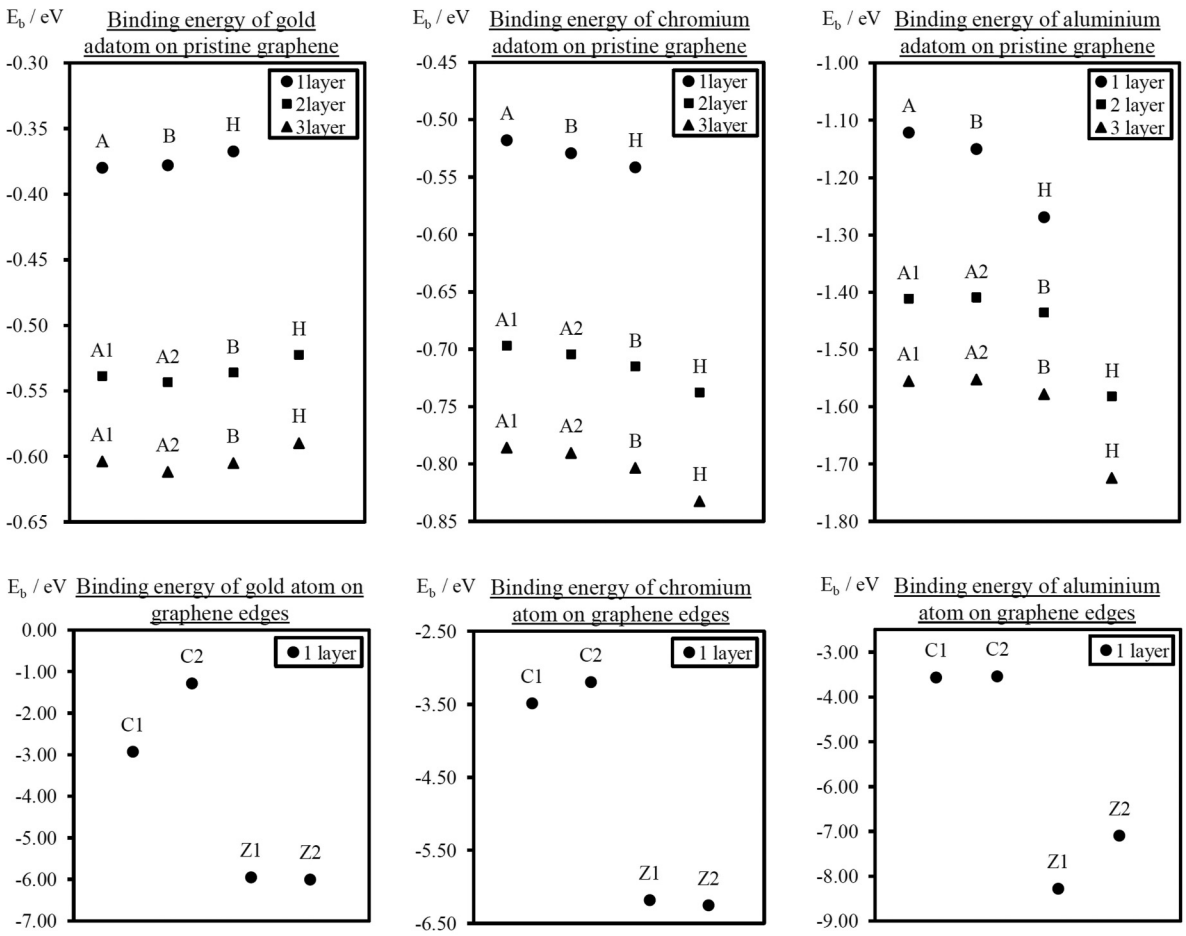

FIG. 6. The calculated binding energy for metal atoms adsorbed on the pristine substrates and bound at monolayer edge sites. The energetic ordering of the adsorption sites is seen to remain the same for increasing thicknesses. See Fig. 3 for nomenclature of binding sites.

were nominated because they comprise sites which give the lowest combination of binding energies which can be joined by a path traversing the entire unit cell. The established linear/quadratic synchronous transit (LST/QST) scheme of Halgren and Lipscomb[70] for determining reaction pathways, as modified to include conjugate gradient refinements and generalized to include periodic systems by Govind *et al.*[71] and implemented in CASTEP[60] was used to locate the transition state configurations and thus evaluate the adatom migration activation barriers associated with these paths. The reactant and product states were first obtained by carrying out ultrafine geometry optimization calculations with the pertinent adatoms at the path endpoints as indicated for the supercells illustrated in Fig. 5. The reaction trajectory joining these reactant and product states was initially guessed by using the LST interatomic distance interpolation scheme,[70] and the midpoint of this trajectory was used as the intermediate state to define the initial three-point QST pathway. A series of conjugate gradient minimizations and QST cycles were carried out from this point to locate the energy saddle point until the root mean square (rms) of all atomic forces was converged to within 0.05 eV $Å^{-1}$. All other calculation input parameters were the same as in Sec. II B. The resulting energy barriers are tabulated in Table III.

III. RESULTS AND DISCUSSION

A. Binding energies and metal-carbon bond distances at absolute zero from *ab initio* data

All metal adatoms and edge atoms settled onto the sites they were initially placed into, confirming that local energy minima exist for all configurations studied. The calculated binding energies E_b corresponding to the fully optimized configurations are tabulated in Table II and plotted in Fig. 6. Figure 7 shows total electron density slices for Au adsorbed onto monolayer and trilayer graphene, and bound to the monolayer edge sites C_1, C_2, Z_1, and Z_2. For all adsorption states for all metals, structural perturbations to the graphene lattice were small, as Fig. 7 shows for the case of Au. The adsorption bonding character is seen to be consistent with physisorption. The increased adsorption energy for the trilayer case is evident from the smaller Au-graphene surface distance and the increased electron density between the Au and the binding carbon atom. In contrast, the binding energies at monolayer edge sites are much higher than the adsorption energies in all cases, confirming that these defect sites are much more stable, consistent with our STEM observations. These results are clearly supported by Fig. 7, which shows a substantial region of electron density in between the C and Au at the edge sites, which warrants interpretation as a substantially stronger bond.

In Table II, three distances are tabulated for the adsorption calculations: (i) the distance(s) along the binding direction(s) from the adatom to the nearest carbon atoms (1 for sites A, A_1, and A_2, 2 for site B, and 6 for site H), (ii) the distance along the z direction from the adatom to the nearest carbon atom(s), and (iii) the distance along the z axis from the adatom to the fixed carbon atoms of the top layer. The difference between the latter two of these three distances is equal to the amount by which the top graphene layer had puckered out-of-plane. These puckering distances are all small, indicating that all metal adatoms do little to interfere with the structural integrity of the lattice. The binding energies are seen to significantly increase for increasing layer numbers for all of the metals tested, adding credibility to the notion that the van der Waals interaction with the sublayers accounts for a significant proportion of the metal-graphene binding energy in real laboratory samples. For each and every adsorption site and metal studied, the energy difference between the two and three layer cases is smaller than the difference between the one and two layer cases. This certainly seems like an intuitive result and it suggests that the binding energy converges towards that of the bulk graphite (0001) surface as the thickness is increased beyond three layers. Further calculations for higher numbers of graphene layers could be carried out to predict the thickness required to recover the behavior of the bulk graphite (0001) surface, although it may be wise to resort to using symmetry finders to make such calculations computationally efficient, depending on the scaling behavior of the code used.

A further important conclusion of the results is that the absolute difference in binding energy between the A_1, A_2, B, and H adsorption sites remains unchanged for the various studied thicknesses. This is evident from the energy trends in Fig. 6, in which it can be seen that the two layer and three layer data points for a given metal are all approximately related by a rigid translation along the energy axis. So despite the proportional contribution of the sublayers to the total binding energy being very significant, the energetic ordering of the adsorption sites is actually predicted to be independent of the thickness. This indicates that at absolute zero, the short-range carbon-metal binding occurring on the top layer takes precedence over the van der Waals contribution from the sublayers, giving rise to static configurations for which the energetically favored adsorption site is unchanged, irrespective of how thick the sample is.

B. Adatom mobility supported by *ab initio* results and observed using STEM

Despite the prediction that stable configurations exist for all metals and sites at 0 K, this is in contrast to our STEM observations[32–35] at room temperature, $T \sim 300$ K. We now argue that our migration activation barrier calculations summarized in Table III strongly support the notion that thermal effects cause the adatoms to be mobile along in-plane directions. Room temperature corresponds to a fundamental temperature of $k_BT = 0.026$ eV (3 d.p.), where k_B is the Boltzmann constant. The magnitude of the metal-carbon binding energy in all cases is much larger than k_BT at room temperature, so an argument based on thermal bond breaking cannot be invoked to account for the continual absence of adatoms on clean regions. However, the migration activation barriers presented in Table III for the case of monolayer substrates at 0 K are well below k_BT for Au and Cr at $T \sim 300$ K, indicating that these adatoms are likely to be extremely mobile on all the substrates studied at room temperature. For Al, the activation barriers are between 0.166

TABLE II. (Ad)atom binding energies metal-carbon distances associated with the fully relaxed structures. The differences between values in the two rightmost columns indicate the graphene lattice puckering distance in each adsorption case. Distances which are identical by definition are boldface. See Fig. 3 for nomenclature of binding sites.

Metal/graphene system	Site	Binding energy, E_b/eV (3 d.p.)	Distance from metal (ad)atom to nearest carbon atom(s) along bond direction(s)/Å (3 d.p.)	Distance along z axis from metal adatom to nearest carbon atom(s)/Å (3 d.p.)	Distance along z axis from metal adatom to fixed top layer carbon atoms/Å (3 d.p.)
Au					
One layer adsorption sites	A	− 0.380	**3.082**	**3.082**	3.095
	B	− 0.378	3.291	3.215	3.217
	H	− 0.367	3.700	3.421	3.408
Two layer adsorption sites	A_1	− 0.539	**3.008**	**3.008**	3.025
	A_2	− 0.543	**2.661**	**2.661**	2.731
	B	− 0.536	3.283	3.207	3.209
	H	− 0.522	3.665	3.383	3.379
Three layer adsorption sites	A_1	− 0.604	**2.729**	**2.729**	2.807
	A_2	− 0.612	**2.702**	**2.702**	2.765
	B	− 0.605	3.233	3.156	3.159
	H	− 0.590	3.650	3.366	3.360
One layer edge sites	C_1	− 2.927	2.125	–	–
	C_2	− 1.284	2.154	–	–
	Z_1	− 5.950	2.171	–	–
	Z_2	− 6.003	2.004	–	–
Cr					
One layer adsorption sites	A	− 0.518	**2.299**	**2.299**	2.322
	B	− 0.529	2.359	2.250	2.264
	H	− 0.542	2.499	2.056	2.063
Two layer adsorption sites	A_1	− 0.697	**2.295**	**2.295**	2.308
	A_2	− 0.704	**2.288**	**2.288**	2.299
	B	− 0.715	2.356	2.247	2.254
	H	− 0.738	2.493	2.049	2.048
Three layer adsorption sites	A_1	− 0.786	**2.284**	**2.284**	2.300
	A_2	− 0.790	**2.279**	**2.279**	2.291
	B	− 0.803	2.344	2.231	2.243
	H	− 0.832	2.473	2.025	2.020
One layer edge sites	C_1	− 3.485	2.036	–	–
	C_2	− 3.090	1.942	–	–
	Z_1	− 6.181	1.827	–	–
	Z_2	− 6.252	1.893	–	–
Al					
One layer adsorption sites	A	− 1.121	**2.277**	**2.277**	2.241
	B	− 1.150	2.347	2.236	2.235
	H	− 1.269	2.563	2.127	2.135
Two layer adsorption sites	A_1	− 1.411	**2.270**	**2.270**	2.220
	A_2	− 1.409	**2.272**	**2.272**	2.230
	B	− 1.435	2.349	2.239	2.215
	H	− 1.582	2.568	2.135	2.133
Three layer adsorption sites	A_1	− 1.555	**2.271**	**2.271**	2.222
	A_2	− 1.552	**2.272**	**2.272**	2.212
	B	− 1.578	2.349	2.240	2.216
	H	− 1.724	2.570	2.137	2.133
One layer edge sites	C_1	− 3.564	2.002	–	–
	C_2	− 3.539	1.892	–	–
	Z_1	− 8.280	1.976	–	–
	Z_2	− 7.095	1.935	–	–

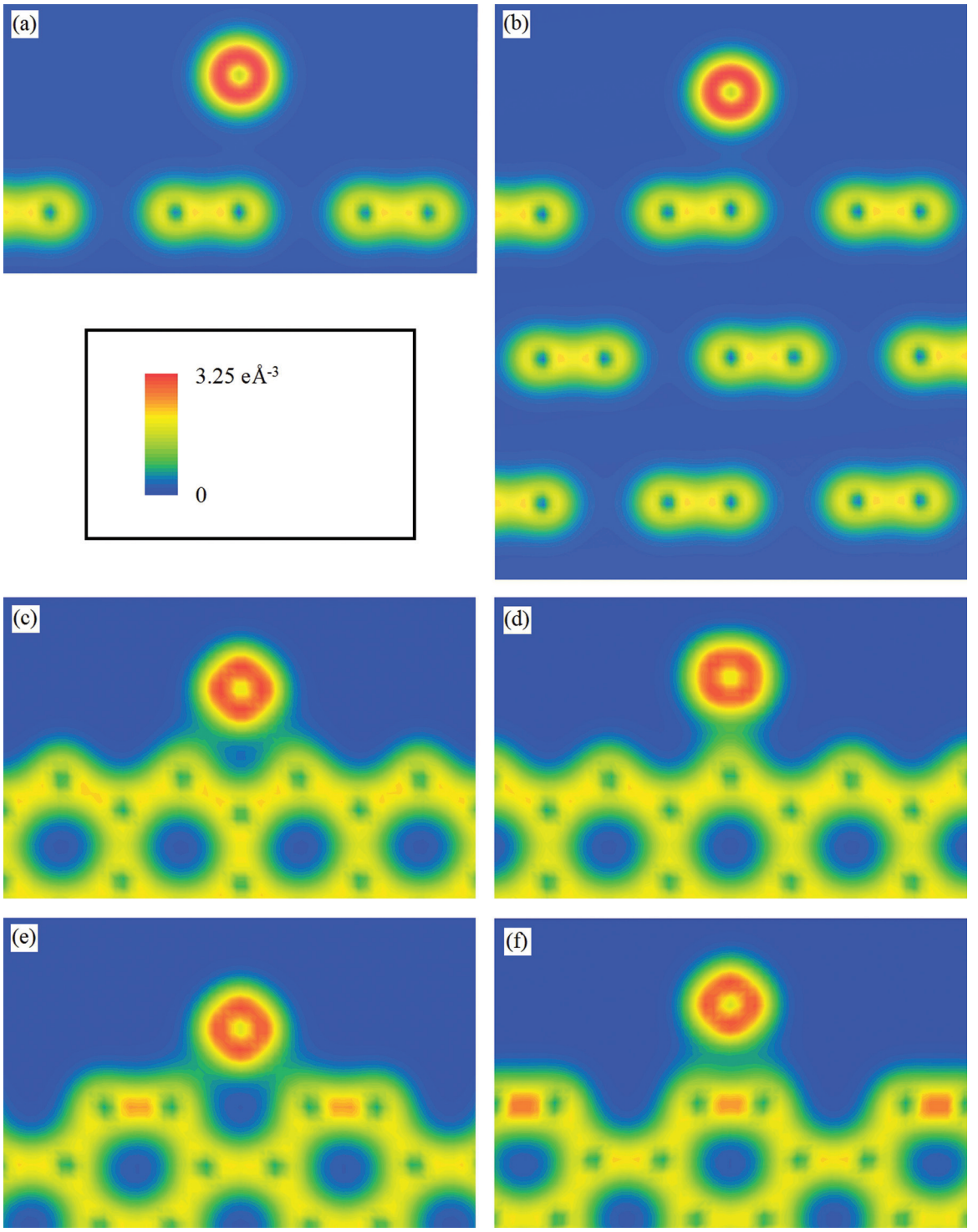

FIG. 7. (Color online) Electron density images showing the difference in bonding character between adsorption and edge sites for Au. (a) Cross section of the total electron density field shown in color units of electrons $/\text{Å}^3$ for Au at adsorption site A for the fully relaxed monolayer. (b) Corresponding trilayer image, showing Au at site A_1. The cross sections shown intersect the graphene along the "armchair" direction, thus showing the carbon-carbon bonds for comparison. The bonding character is seen to be consistent with physisorption in both cases, though a slightly more substantial bond is evident for the trilayer case. Au atom binding to the edge sites (c) Z_1 (d) Z_2 (e) C_1, and (f) C_2. Clear and substantial regions of electron density are observable in all four cases, consistent with a stronger metal carbide bond. See Fig. 3 for nomenclature of binding sites.

and 0.197 eV (3 d.p.), within one order of magnitude of $k_B T$. This suggests that Al adatoms are likely to migrate at a slower rate than Au and Cr, although the barrier is nonetheless trivially small. Our results predict that lattice edge sites would result in significantly stronger adatom binding than the pristine, clean regions of the lattice. This is demonstrated very clearly by our

TABLE III. Calculated migration barriers for Au, Cr, and Al on the lowest energy migration pathways on pristine monolayer, bilayer, and trilayer graphene.

Adatom	Substrate	Path	Migration barrier ΔE/eV (3 d.p.)
Au	One layer	$A \rightarrow B \rightarrow A$	0.007
	Two layer	$A_1 \rightarrow B \rightarrow A_2$	0.008
		$A_2 \rightarrow B \rightarrow A_1$	0.024
	Three layer	$A_1 \rightarrow B \rightarrow A_2$	0.019
		$A_2 \rightarrow B \rightarrow A_1$	0.025
Cr	One layer	$H \rightarrow B \rightarrow H$	0.022
	Two layer	$H \rightarrow B \rightarrow H$	0.021
	Three layer	$H \rightarrow B \rightarrow H$	0.022
Al	One layer	$H \rightarrow B \rightarrow H$	0.166
	Two layer	$H \rightarrow B \rightarrow H$	0.178
	Three layer	$H \rightarrow B \rightarrow H$	0.197

recent STEM observations presented in Fig. 1. We note that one recent study[72] used DFT to predict binding energies of Au atoms at different types of edge site to be between 3.1 and 6.4 eV, in good agreement with our values. Thus, we conclude that all adatoms in our samples had migrated across the clean regions of the lattice into more stable defective or contaminated regions within a short timeframe as a result of the statistical inevitability associated with perturbing thermal effects at $T \sim 300$ K. This migration occurred because of the small adatom migration barriers for samples of all thicknesses.

C. Comments on possible effects of the electron beam in our samples

We need to also consider the effect of the STEM electron beam on our specimens. A very small number of Au atoms were observed by STEM on clean regions some time after deposition of the adatoms. While our published STEM images confirm that the beam does little or nothing to affect the integrity of the graphene itself at 60 keV, it is necessary to rationalize the circumstances whereby single metals are observed on clean regions of graphene. In most instances, regardless of specimen thickness and the metal species, the adatoms exist as clusters at defected or hydrocarbon contaminated regions of the sample. This can be understood by the high mobility of the adatoms, and the greater energetic stability of adatom binding at these sites. We conjecture that in cases where Au atoms were observed by STEM on clean thicker regions,[32] the beam may have displaced these Au atoms from clusters in the more stable regions during the scanning process. Considerations based on a recent quantitative study of beam damage in graphene[73] could be used to test these remarks. This is not to suggest we do not recognize the possibility of knock-on damage in our microscopy experiments, local heating effects (which are arguably negligible[74]) or the temporary localized accumulation of negative charge around the beam. These effects were not however explicitly considered in this study. In summary, we consider migration effects to be the pivotal reason why adatoms are not generally observed on clean graphene regions, with electron beam knock-on effects being a secondary consideration. Indeed, the beam itself is attributed as a possible reason for the observation of single Au atoms on clean regions due to displacement effects.

IV. CONCLUSIONS

We have presented DFT calculations for the binding energy of Au, Al, and Cr atoms bound at graphene edge sites and adsorbed on monolayer, bilayer, and trilayer graphene using the van der Waals-correction scheme of Tkatchenko and Scheffler[42] for the first time. The contribution to the total binding energy from graphene sublayers was predicted to be very significant, although the edge binding energies were found to be substantially higher for all atoms in all cases. Migration activation barriers for these adatoms on monolayer, bilayer, and trilayer graphene were then calculated and shown to be smaller than or within one order of magnitude of $k_B T$ at room temperature in all cases, implying that these adatoms are extremely mobile on graphene at room temperature. It was concluded from this that graphene samples doped with Au, Cr, and Al should be seen to be completely devoid of these dopants on the pristine regions, with the dopants binding preferentially to the edge defect sites. This was shown to be in striking agreement with the STEM data presented in Fig. 1 of this study, along with our recently published STEM observations.[32–35] Additionally, a brief review of atomic position fixing conventions adopted in recently published calculations was presented, and a simple guiding principle based on lattice symmetries was suggested for future studies.

ACKNOWLEDGMENTS

T.P.H. would like to thank the UK EPSRC for the Doctoral Training Award which funded this research. We acknowledge use of Hartree Centre resources in this work. The STFC Hartree Centre is a research collaboration in association with IBM providing High Performance Computing platforms funded by the UK's investment in e-Infrastructure. The Centre aims to develop and demonstrate next generation software, optimized to take advantage of the move towards exa-scale computing. Additional high performance computing facilities were provided by the ARC1 resource at the University of Leeds. SuperSTEM is the UK EPSRC National Facility

for Aberration-Corrected Scanning Transmission Electron Microscopy.

APPENDIX: OPTIMIZATION OF ISOLATED STRUCTURES AND ENERGY/ENTHALPY CONVERGENCE WITH CELL DIMENSIONS—FURTHER INFORMATION

The single layer graphene unit cell shown in Fig. 8(a) was constructed, whose initial in-plane lattice vectors $\vec{a}_{1l}^{(i)}$ and $\vec{b}_{1l}^{(i)}$ were left unconstrained and both set initially at the experimentally measured[63] bulk graphite value of 2.461 Å. This unit cell was then duplicated, and the vacuum-direction lattice vector $\vec{c}_{1l}^{(i)}$ was fixed at magnitudes increasing in 1 Å increments from $|\vec{c}_{1l}^{(i)}| = 2, \ldots, 16$ Å inclusive, to make a total of 15 unit cells. In all of these, the carbon layer was placed in the center of the vacuum slab at fractional coordinate $0.5|\vec{c}_{1l}^{(i)}|$. A geometry optimization calculation was carried out on each of these, in which the atomic positions and lengths $|\vec{a}_{1l}^{(i)}|$ and $|\vec{b}_{1l}^{(i)}|$ were relaxed, all unit cell angles were fixed, and $|\vec{c}_{1l}^{(i)}|$ was fixed at the value appropriate to each case. The fully optimized TS-corrected enthalpies were plotted against the vacuum thickness $|\vec{c}_{1l}^{(i)}|$ to serve two purposes. First, to identify the smallest value of $|\vec{c}_{1l}^{(i)}|$ for which the undesired intercellular interlayer interaction in the vacuum direction had converged to zero. This value of $|\vec{c}_{1l}^{(i)}|$ was named $|\vec{c}_{1l}|$ and identified as $|\vec{c}_{1l}| = 12$ Å. Second, it served to calculate the carbon-carbon bond lengths as optimized using the particular choice of functional, along with the corresponding optimized values of $|\vec{a}_{1l}^{(i)}|$ and $|\vec{b}_{1l}^{(i)}|$. These values were named $|\vec{a}_{1l}|$ and $|\vec{b}_{1l}|$, respectively, and recorded at values $|\vec{a}_{1l}| = |\vec{b}_{1l}| = 2.459$ Å (4 s.f.). A similar procedure was then repeated for the case of two layer and three layer graphene on the multilayer unit cell shown in Fig. 8(b), in which the top carbon layer was placed at the center of the vacuum similar to above. From similarly designed geometry optimization calculations, the minimum required vacuum thicknesses for the two and three layer cases, $|\vec{c}_{2l}|$ and $|\vec{c}_{3l}|$, were identified as $|\vec{c}_{2l}| = 16$ Å and $|\vec{c}_{3l}| = 20$ Å. The corresponding in-plane lattice parameters were found to be $|\vec{a}_{2l}| = |\vec{b}_{2l}| = 2.457$ Å (4 s.f.) and $|\vec{a}_{3l}| = |\vec{b}_{3l}| = 2.456$ Å (4 s.f.), and the corresponding optimized interlayer spacings were found to be $d_{s(2l)} = 3.360$ Å (4 s.f.) and $d_{s(3l)} = 3.354$ Å (4 s.f.).

Next, vacuum-filled cubic supercells were constructed containing a metal atom placed directly in the center as shown in Fig. 8(c). Each supercell had lattice parameters fixed at values of $|\vec{A}_m| = |\vec{B}_m| = |\vec{C}_m|$ with $m = \mathrm{Au}, \mathrm{Al}, \mathrm{Cr}$ as appropriate, with $|\vec{A}_m|$ increasing (along with $|\vec{B}_m|$ and $|\vec{C}_m|$) in 1 Å increments from 2 to 15 Å inclusive, to make a total of $14 \times 3 = 42$ cubic supercells. TS-corrected zero-point energy calculations were carried out for each, and the supercell energies were converged with respect to the supercell size in order to decouple the intercellular metal-metal interactions. The minimum supercell size required to satisfy the decoupling condition all metals was identified as $|\vec{A}_m| = |\vec{B}_m| = |\vec{C}_m| = 10$ Å.

The supercell shown in Fig. 8(d) was then constructed by forming a 2×2 array of the fully optimized single graphene layer unit cells shown in Fig. 8(a). The supercell lattice vectors

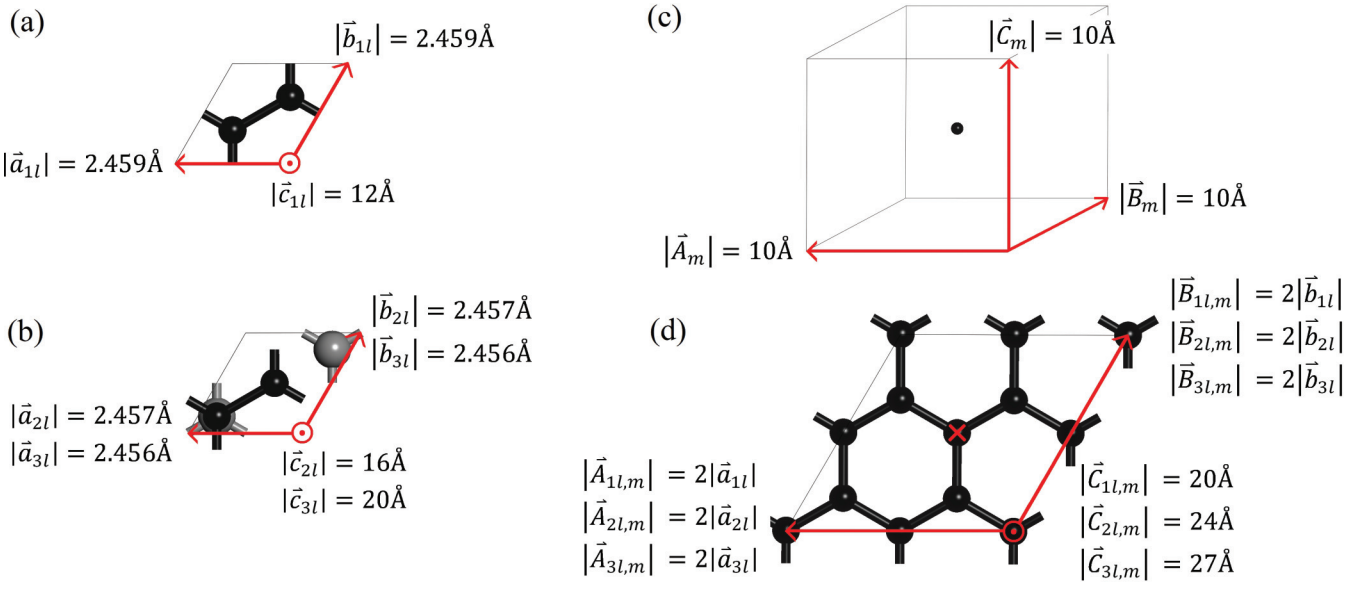

FIG. 8. (Color online) (a) Fully optimized graphene unit cell with relaxed lattice parameters in red. Atoms and bonds are represented by balls and sticks, respectively. (b) Fully optimized multilayer graphene unit cell, as in (a). To aid visualization, the atoms and bonds of the first sublayer are represented with large gray balls and sticks, and those of the top layer with small black balls and sticks. The second sublayer is not indicated owing to the assumed AB stacking structure. (c) Isolated metal atom cubic supercell. The lattice parameters shown indicate the smallest supercell size required to decouple all intercellular metal-metal interactions. (d) Graphene + metal supercell spanning 2×2 unit cells. The lattice parameters shown indicate the vacuum thicknesses required to decouple intercellular interactions along the vacuum direction only.

were fixed at values $\vec{A}_{1l,m} = 2\vec{a}_{1l}$ and $\vec{B}_{1l,m} = 2\vec{b}_{1l}$, and the vacuum-direction lattice parameter $\vec{C}^{(i)}_{1l,m}$ was initially fixed at magnitudes increasing in 1 Å increments from $|\vec{C}^{(i)}_{1l,m}| = 6, \ldots, 27$ Å inclusive, to make 22 supercells. Into each of these 22 supercells, a metal atom of species $m = \mathrm{Au, Al, Cr}$ was placed 2 Å directly above the central carbon atom as indicated in Fig. 8(d) by the red cross, thus creating a total of $22 \times 3 = 66$ supercells. In each one of these supercells, the carbon layer was fixed at the center of the vacuum at fractional coordinate $0.5|\vec{C}^{(i)}_{1l,m}|$. TS-corrected zero-point energy calculations were carried out with the self-consistent electrostatic dipole correction scheme of Neugebaueur and Scheffler[53] and the energy was plotted vs $|\vec{C}^{(i)}_{1l,m}|$ for each. This served the purpose of establishing the minimum vacuum thickness required to converge both intercellular interactions in the direction $\vec{C}^{(i)}_{1l,m}$ and spurious intercellular dipole-dipole interactions to zero. The smallest value of $|\vec{C}^{(i)}_{1l,m}|$ for which the energy plots were deemed to have converged for all metals was named $|\vec{C}_{1l,m}|$ and identified as $|\vec{C}_{1l,m}| = 20$ Å. A similar procedure was repeated for the two and three layer cases using the optimized interlayer spacings determined above. The top carbon layer was again fixed at the center of the vacuum and the corresponding required vacuum thicknesses were found to be $|\vec{C}_{2l,m}| = 24$ Å and $|\vec{C}_{3l,m}| = 27$ Å.

Three single layer supercells were constructed from 3×3, 4×4, and 5×5 arrays of the fully relaxed unit cells from Fig. 8(a), whose vacuum-direction lattice vector $\vec{C}_{1l}$ fixed at the value $\vec{C}_{1l} = 20$ Å in all cases. This vacuum thickness was chosen so as to meet the requirements of the individual convergence tests just described; i.e., $|\vec{C}_{1l}| = |\vec{C}_{1l,m}| > |\vec{c}_{1l}|$.

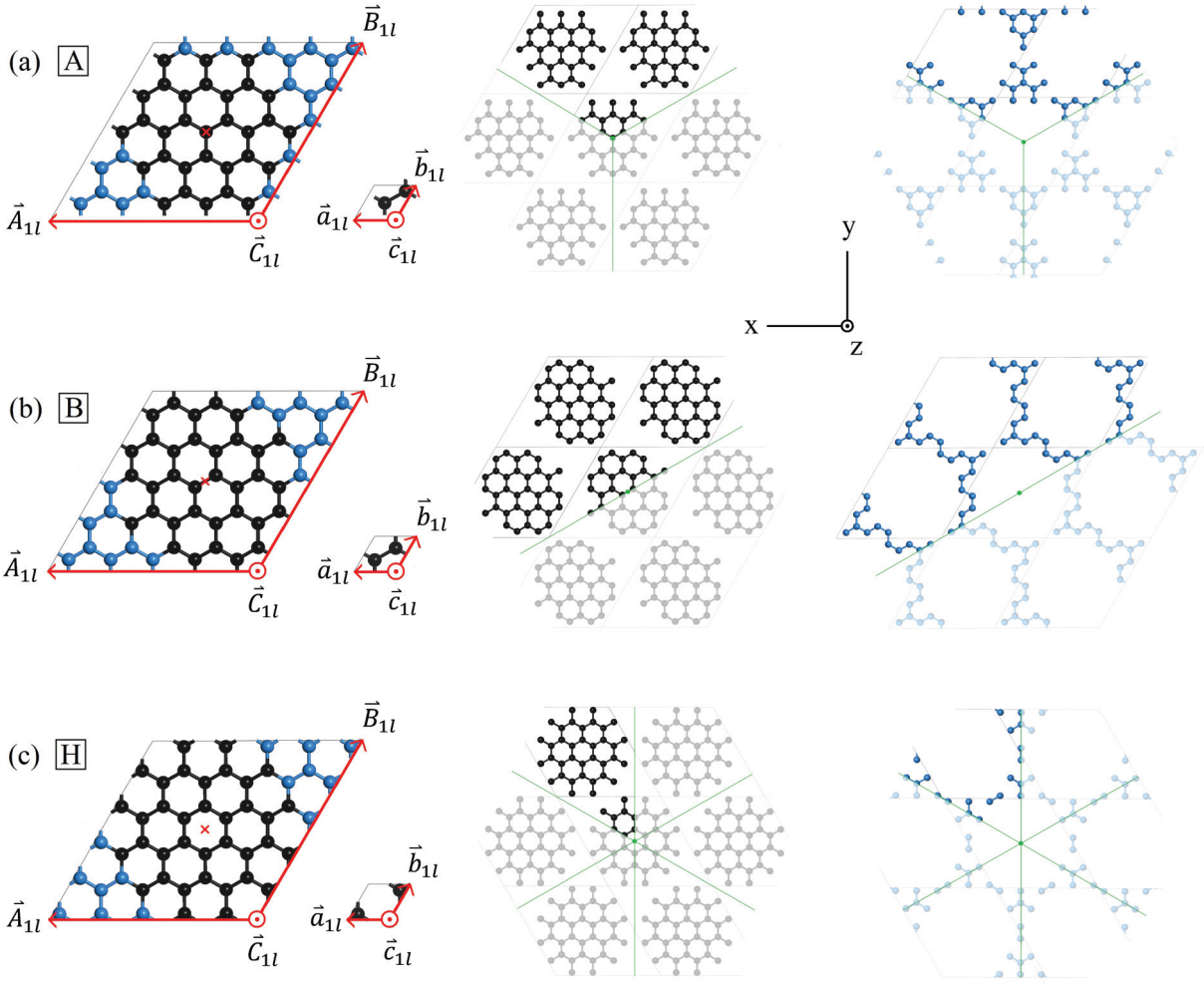

FIG. 9. (Color online) The three single layer supercells before geometry optimization used for the adatom + graphene systems for (a) site A, (b) site B, and (c) site H. In all cases, carbon atoms whose positions are fixed are represented in blue and those whose positions are relaxed are represented in black. The corresponding unfixed and fixed sublattices are displayed to the right of their corresponding supercells, in which the green lines show boundaries between segments of the lattice which are equivalent by virtue of rotational symmetry about the axis passing through the adsorption site represented by the green dot in the center. The red cross denotes the initial adatom location. $|\vec{a}_{1l}| = |\vec{b}_{1l}| = 2.459$ Å (3 d.p.), $|\vec{A}_{1l}| = |\vec{B}_{1l}| = 5|\vec{a}_{1l}| = 12.293$ Å (3 d.p.), and $|\vec{C}_{1l}| = |\vec{c}_{1l}| = 20$ Å. See Fig. 3 for nomenclature on adsorption sites.

A metal atom of species m was placed 2 Å above the central carbon atom for each of these three supercells, with m = Au, Al, and Cr as appropriate, thereby producing a total of $3 \times 3 = 9$ supercells. TS-corrected zero-point energy calculations were carried out for these nine systems and the total energy was plotted against supercell size for each metal to identify the minimum size required to decouple all intercellular adatom interactions. The 5×5 supercells with lattice parameters $|\vec{A}_{1l}| = |\vec{B}_{1l}| = 5|\vec{a}_{1l}|$ were deemed sufficient for this purpose. It was also verified that this choice satisfied the intercellular metal-metal convergence requirement established above since $|\vec{A}_{1l}| > |\vec{A}_m|$. No similar

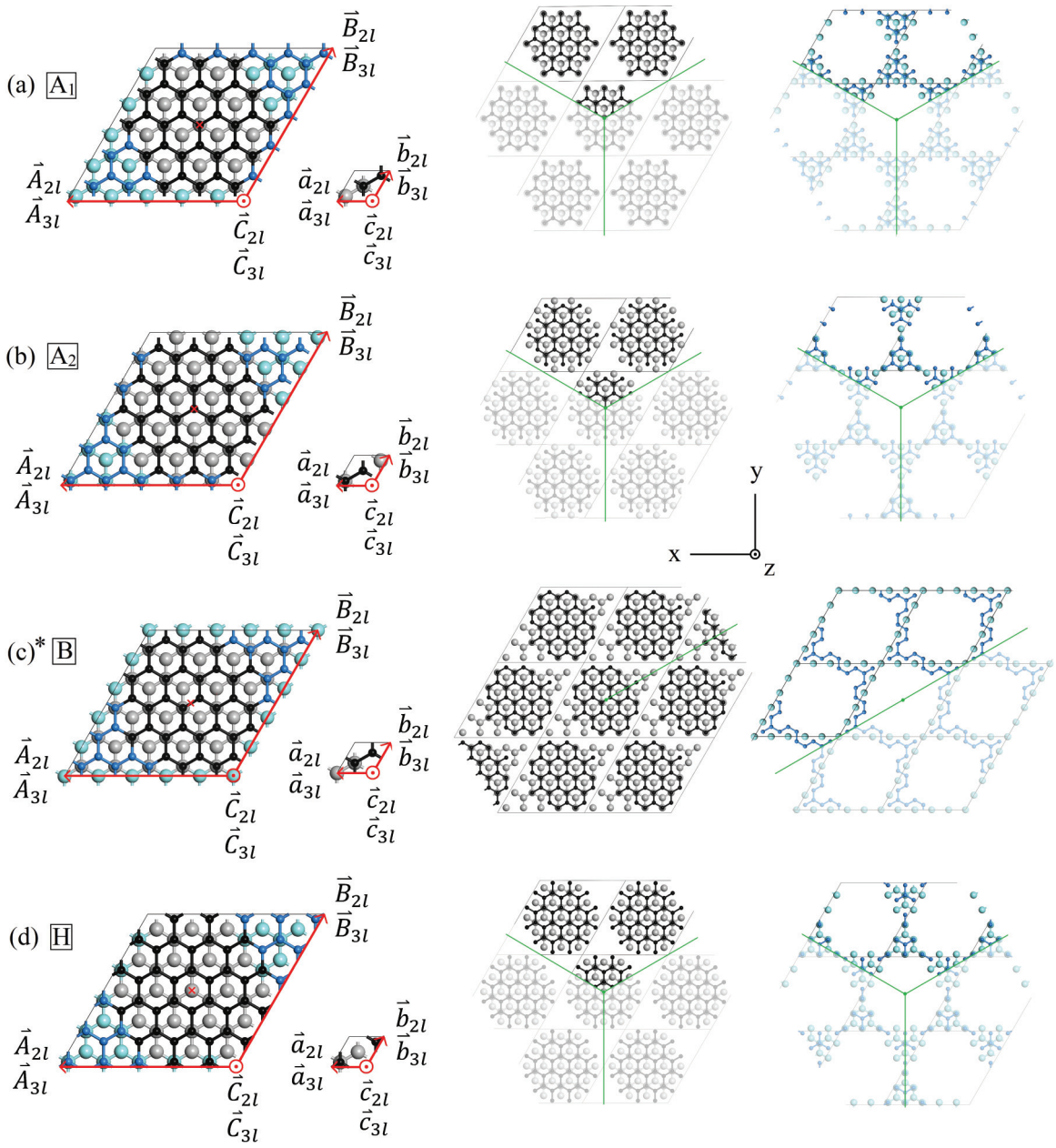

FIG. 10. (Color online) The multilayer input supercells for (a) site A_1, (b) site A_2, (c) site B, and (d) site H. The top carbon layer is represented by small balls and sticks, and the first sublayer is represented by large balls and sticks. No further sublayers are indicated owing to the assumed AB stacking structure. Fixed top layer and sublayer C atoms are blue and light green, respectively. Unfixed top layer and sublayer C atoms are colored black and gray, respectively. As in Fig. 9, the red cross denotes the initial adatom location. As in Fig. 9, the unfixed and fixed sublattices are shown on the right of their corresponding supercell, divided into segments which are equivalent by rotational symmetry about the axis passing through the adsorption site. $|\vec{a}_{2l}| = |\vec{b}_{2l}| = 2.457$ Å (3 d.p.), $|\vec{A}_{2l}| = |\vec{B}_{2l}| = 5|\vec{a}_{2l}| = 12.283$ Å (3 d.p.), $|\vec{C}_{2l}| = |\vec{c}_{2l}| = 24$ Å, $|\vec{a}_{3l}| = |\vec{b}_{3l}| = 2.456$ Å (3 d.p.), $|\vec{A}_{3l}| = |\vec{B}_{3l}| = 5|\vec{a}_{3l}| = 12.280$ Å (3 d.p.), and $|\vec{C}_{3l}| = |\vec{c}_{3l}| = 27$ Å. *The B site in (c) is the only site for which the rotational symmetry of the first sublayer (and also therefore the complete lattice) is onefold. For this case, C positions were fixed on the supercell perimeter on the first sublayer in preference to some other arbitrary selection resulting in onefold symmetry, resulting in the twofold fixed sublattice rotational symmetry shown. See Fig. 3 for nomenclature on adsorption sites.

test of in-plane supercell sizes for multilayer + metal systems was carried out owing to the extensive computational cost involved. Supercell sizes of 5×5 unit cells were used for two and three layer cases, with $|\vec{A}_{2l}| = |\vec{B}_{2l}| = 5|\vec{a}_{2l}|$ and $|\vec{C}_{2l}| = 24$ Å for the two layer system and $|\vec{A}_{3l}| = |\vec{B}_{3l}| = 5|\vec{a}_{3l}|$ and $|\vec{C}_{3l}| = 27$ Å for the three layer system, with the top carbon layer once again placed in the center of the vacuum. Measures taken to estimate the error in the calculated binding energies due to lattice perturbations under relaxation and the limited size of the 5×5 supercells are outlined in Sec. II B (Figs. 9 and 10).

For the monolayer edge binding supercells, graphene edge slab/vacuum supercells akin to those shown in Fig. 4 were prepared, in which metal atoms of species $m = \mathrm{Au, Al, Cr}$ were placed initially at each end of the slab in the graphene plane as indicated by the red crosses at an initial distance of 2 Å from the nearest C atom(s). For the zigzag edge slabs, a series of geometry optimization calculations was carried out in order to converge the total relaxed TS-corrected system enthalpy with respect to the slab width $\vec{A}_{1l,\mathrm{zigzag}}$, and the slab thickness + vacuum thickness, whose sum is denoted $\vec{B}_{1l,\mathrm{zigzag}}$. The intercellular layer spacings were fixed at the value $|\vec{C}_{1l}| = 20$ Å, thus satisfying the test described earlier. The total binding energy was deemed to have converged for arrays of 5×8 of the appropriate unit cells for sites Z_1 and Z_2. In an identical manner, an array of 5×7 appropriate unit cells for sites C_1 and C_2 was deemed sufficient. The vacuum thickness in both cases was set at 20 Å. Example supercells are illustrated in Fig. 4. Recent work has suggested possible reconstruction at graphene edges,[75] however this extra detail was not deemed necessary for this work.

For all calculations in this section, the exit criterion was defined as a total change in system energy of $< 5 \times 10^{-3}$ eV between successive calculations.

*Corresponding author: pmth@leeds.ac.uk
†Corresponding author: a.j.scott@leeds.ac.uk

[1] K. S. Novoselov, A. K. Geim, S. V. Morozov, D. Jiang, Y. Zhang, S. V. Dubonos, I. V. Grigorieva, and A. A. Firsov, Science **306**, 666 (2004).
[2] F. Schwierz, Nat. Nanotechnol. **5**, 487 (2010).
[3] Y. Wu, V. Perebeinos, Y.-M. Lin, T. Low, F. Xia, and P. Avouris, Nano Lett. **12**, 1417 (2012).
[4] K. Nagashio, T. Nishimura, K. Kita, and A. Toriumi, Jpn. J. Appl. Phys. **49**, 051304 (2010).
[5] K. Nagashio, T. Nishimura, K. Kita, and A. Toriumi, Appl. Phys. Lett. **97**, 143514 (2010).
[6] S. Russo, M. F. Craciun, M. Yamamoto, A. F. Morpurgo, and S. Tarucha, Physica E **42**, 677 (2010).
[7] P. A. Khomyakov, A. A. Starikov, G. Brocks, and P. J. Kelly, Phys. Rev. B **82**, 115437 (2010).
[8] R. S. Sundaram, M. Steiner, H.-Y. Chiu, M. Engel, A. A. Bol, R. Krupke, M. Burghard, K. Kern, and P. Avouris, Nano Lett. **11**, 3833 (2011).
[9] M.P. Lima, A. J. R. da Silva, and A. Fazzio, Phys. Rev. B **84**, 245411 (2011).
[10] J. Ding, Z. Qiao, W. Feng, Y. Yao, and Q. Niu, Phys. Rev. B **84**, 195444 (2011).
[11] H. Valencia, A. Gil, and G. Frapper, J. Phys. Chem. C **114**, 14141 (2010).
[12] R. Varns and P. Strange, J. Phys.: Condens. Matter **20**, 225005 (2008).
[13] M. Sargolzaei and F. Gudarzi, J. Appl. Phys. **110**, 064303 (2011).
[14] K. Nakada and A. Ishii, Solid State Commun. **151**, 13 (2011).
[15] C. Cao, M. Wu, J. Jiang, and H.-P. Cheng, Phys. Rev. B **81**, 205424 (2010).
[16] A. Ishii, M. Yamamoto, H. Asano, and K. Fujiwara, J. Phys.: Conf. Ser. **100**, 052087 (2008).
[17] K.T. Chan, J. B. Neaton, and M. L. Cohen, Phys. Rev. B **77**, 235430 (2008).
[18] M. Amft, S. Lebègue, O. Eriksson, and N. V. Skorodumova, J. Phys.: Condens. Matter **23**, 395001 (2011).
[19] Z. M. Ao, Q. Jiang, R. Q. Zhang, T. T. Tan, and S. Li, J. Appl. Phys. **105**, 074307 (2009).
[20] L. Hu, X. Hu, X. Wu, C. Du, Y. Dai, and J. Deng, Physica B **405**, 3337 (2010).
[21] H. Johll, H. C. Kang, and E. S. Tok, Phys. Rev. B **79**, 245416 (2009).
[22] Y. Mao, J. Yuan, and J. Zhong, J. Phys.: Condens. Matter **20**, 115209 (2008).
[23] O. V. Yazyev and A. Pasquarello, Phys. Rev. B **82**, 045407 (2010).
[24] K.H. Jin, S. M. Choi, and S. H. Jhi, Phys. Rev. B **82**, 033414 (2010).
[25] Y. Tang, Z. Yang, and X. Dai, J. Chem. Phys. **135**, 224704 (2011).
[26] D. W. Boukhvalov and M. I. Katsnelson, Appl. Phys. Lett. **95**, 023109 (2009).
[27] S. Malola, H. Hakkinen, and P. Koskinen, Appl. Phys. Lett. **94**, 043106 (2009).
[28] E. J. G. Santos, A. Ayuela, and D. Sánchez-Portal, New J. Phys. **12**, 053012 (2010).
[29] O. Cretu, A. V. Krasheninnikov, J. A. Rodriguez-Manzo, L. Sun, R. M. Nieminen, and F. Banhart, Phys. Rev. Lett. **105**, 196102 (2010).
[30] E. J. G. Santos, D. Sánchez-Portal, and A. Ayuela, Phys. Rev. B **81**, 125433 (2010).
[31] S. Karoui, H. Amara, C. Bichara, and F. Ducastelle, ACS Nano **4**, 6114 (2010).
[32] R. Zan, Q. M. Ramasse, U. Bangert, and K. S. Novoselov, Nano Lett. **12**, 3936 (2012).
[33] R. Zan, U. Bangert, Q. M. Ramasse, and K. S. Novoselov, Nano Lett. **11**, 1087 (2011).
[34] R. Zan, U. Bangert, Q. M. Ramasse, and K. S. Novoselov, Small **7**, 2868 (2011).
[35] Q. M. Ramasse, R. Zan, U. Bangert, D. W. Boukhvalov, Y.-W. Son, and K. S. Novoselov, ACS Nano **6**, 4063 (2012).
[36] J. P. Perdew, K. Burke, and M. Ernzerhof, Phys. Rev. Lett. **77**, 3865 (1996).
[37] S. Grimme, J. Comput. Chem. **27**,1787 (2006).
[38] H. Rydberg, M. Dion, N. Jacobson, E. Schröder, P. Hyldgaard, S. I. Simak, D. C. Langreth, and B. I. Lundqvist, Phys. Rev. Lett. **91**, 126402 (2003).
[39] M. Dion, H. Rydberg, E. Schröder, D. C. Langreth, and B. I. Lundqvist, Phys. Rev. Lett. **92**, 246401 (2004).
[40] M. Dion, H. Rydberg, E. Schröder, D. C. Langreth, and B. I. Lundqvist, Phys. Rev. Lett. **95**, 109902(E) (2005).

[41]P. Jurečka, J. Černy, P. Hobza, and D. R. Salahub, J. Comput. Chem. **28**, 555 (2007).
[42]A. Tkatchenko and M. Scheffler, Phys. Rev. Lett. **102**, 073005 (2009).
[43]L. G. De Arco, Y. Zhang, A. Kumar, and C. Zhou, IEEE Trans. Nanotechnol. **8**, 135 (2009).
[44]D. Wei, Y. Liu, H. Zhang, L. Huang, B. Wu, J. Chen, and G. Yu, J. Am. Chem. Soc. **131**, 11147 (2009).
[45]A. Malesevic, R. Vitchev, K. Schouteden, A. Volodin, L. Zhang, G. Van Tendeloo, A. Vanhulsel, and C. Van Haesendonck, Nanotechnology **19**, 305604 (2008).
[46]A. Reina, X. Jia, J. Ho, D. Nezich, H. Son, V. Bulovic, M. S. Dresselhaus, and J. Kong, Nano Lett. **9**, 30 (2009).
[47]G. Ming, J. J. Belbruno, S. D. Kenny, and R. Smith, Surf. Sci. **541**, 91 (2003).
[48]T. Eberlein, U. Bangert, R. R. Nair, R. Jones, M. Gass, A. L. Bleloch, K. S. Novoselov, A. Geim, and P. R. Briddon, Phys. Rev. B **77**, 233406 (2008).
[49]J. C. Meyer, A. K. Geim, M. I. Katsnelson, K. S. Novoselov, T. J. Booth, and S. Roth, Nature (London) **446**, 60 (2007).
[50]A. Fasolino, J. H. Los, and M. I. Katsnelson, Nat. Mater. **6**, 858 (2007).
[51]P. Lambin, H. Amara, F. Ducastelle, and L. Henrard, Phys. Rev. B **86**, 045448 (2012).
[52]G. Makov and M. C. Payne, Phys. Rev. B **51**, 4014 (1995).
[53]J. Neugebauer and M. Scheffler, Phys. Rev. B **46**, 16067 (1992).
[54]L. Bengtsson, Phys. Rev. B **59**, 12301 (1999).
[55]L. N. Kantorovich, Phys. Rev. B **60**, 15476 (1999).
[56]P.A. Schultz, Phys. Rev. B **60**, 1551 (1999).
[57]I.-C. Yeh and M. L. Berkowitz, J. Chem. Phys. **111**, 3155 (1999).
[58]T. M. Nymand and P. Linse, J. Chem. Phys. **112**, 6152 (2000).
[59]I. Hamada, M. Otani, O. Sugino, and Y. Morikawa, Phys. Rev. B **80**, 165411 (2009).
[60]S. J. Clark, M. D. Segall, C. J. Pickard, P. J. Hasnip, M. J. Probert, K. Refson, and M. C. Payne, Z. Kristallogr. **220**, 567 (2005).
[61]D. Vanderbilt, Phys. Rev. B **41**, 7892 (1990).
[62]E. R. McNellis, J. Meyer, and K. Reuter, Phys. Rev. B **80**, 205414 (2009).
[63]P. Trucano and R. Chen, J. Chem. Soc., Faraday Trans. 2 **72**, 446 (1976).
[64]H. J. Monkhorst and J. D. Pack, Phys. Rev. B **13**, 5188 (1976).
[65]C. G. Broyden, IMA J. Appl. Math. **6**, 76 (1970).
[66]C. G. Broyden, IMA J. Appl. Math. **6**, 222 (1970).
[67]R. Fletcher, Comput. J. **13**, 317 (1970).
[68]D. Goldfarb, Math. Comput. **24**, 23 (1970).
[69]D. F. Shanno, Math. Comput. **24**, 647 (1970).
[70]T. A. Halgren and W. N. Lipscomb, Chem. Phys. Lett. **49**, 225 (1977).
[71]N. Govind, M. Peterson, G. Fitzgerald, D. K-Smith, and J. Andzelm, Comput. Mater. Sci. **28**, 250 (2003).
[72]H. Wang, K. Li, Y. Cheng, Q. Wang, Y. Yao, U. Schwingenschlögl, X. Zhang, and W. Yang, Nanoscale **4**, 2920 (2012).
[73]J. C. Meyer, F. Eder, S. Kurasch, V. Skakalova, J. Kotakoski, H. J. Park, S. Roth, A. Chuvilin, S. Eyhusen, G. Benner, A. V. Krasheninnikov, and U. Kaiser, Phys. Rev. Lett. **108**, 196102 (2012).
[74]R. F. Egerton, P. Li, and M. Malac, Micron **35**, 399 (2004).
[75]P. Koskinen, S. Malola, and H. Häkkinen, Phys. Rev. Lett. **101**, 115502 (2008).